

GDPO-SR: Group Direct Preference Optimization for One-Step Generative Image Super-Resolution

Qiaosi Yi^{1,2}, Shuai Li¹, Rongyuan Wu^{1,2}, Lingchen Sun^{1,2}, Zhengqiang Zhang^{1,2}, Lei Zhang^{1,2*}

¹The Hong Kong Polytechnic University ²OPPO Research Institute

qiaosiyijoyies@gmail.com, cslzhang@comp.polyu.edu.hk

{novak.li, rong-yuan.wu, ling-chen.sun, zhengqiang.zhang}@connect.polyu.hk

Abstract

Recently, reinforcement learning (RL) has been employed for improving generative image super-resolution (ISR) performance. However, the current efforts are focused on multi-step generative ISR, while one-step generative ISR remains underexplored due to its limited stochasticity. In addition, RL methods such as Direct Preference Optimization (DPO) require the generation of positive and negative sample pairs offline, leading to a limited number of samples, while Group Relative Policy Optimization (GRPO) only calculates the likelihood of the entire image, ignoring local details that are crucial for ISR. In this paper, we propose Group Direct Preference Optimization (GDPO), a novel approach to integrate RL into one-step generative ISR model training. First, we introduce a noise-aware one-step diffusion model that can generate diverse ISR outputs. To prevent performance degradation caused by noise injection, we introduce an unequal-timestep strategy to decouple the timestep of noise addition from that of diffusion. We then present the GDPO strategy, which integrates the principle of GRPO into DPO, to calculate the group-relative advantage of each online generated sample for model optimization. Meanwhile, an attribute-aware reward function is designed to dynamically evaluate the score of each sample based on its statistics of smooth and texture areas. Experiments demonstrate the effectiveness of GDPO in enhancing the performance of one-step generative ISR models. Code: <https://github.com/Joyies/GDPO>.

1. Introduction

Different from classical image super-resolution (ISR) [3, 5, 22, 24, 66, 67], which aims to reconstruct a high-resolution (HR) image from its low-resolution (LR) counterpart with known and relatively simple degradations (e.g., bicubic

downsampling), real-world ISR (Real-ISR) [20, 23, 35, 40, 41, 62] aims to reconstruct HR images from LR inputs captured under real-world conditions, which are often corrupted with complex and unknown degradations. Real-ISR is more ill-posed than classical ISR due to the complex degradation, and the research focuses on how to synthesize realistic details without introducing many visual artifacts. While many GAN-based methods [20, 40, 41, 62] have been proposed for Real-ISR, in recent years, diffusion models [6, 12, 33] have demonstrated significantly stronger capabilities in synthesizing more natural ISR images with richer details [16, 17, 39, 42, 48, 55, 56, 59].

In particular, pre-trained large-scale text-to-image (T2I) diffusion models [19, 34] have been prevalently used as the backbones in Real-ISR tasks due to their powerful generative priors [36, 39, 48, 49, 56, 60, 61, 63]. StableSR [39] firstly adapts the Stable Diffusion (SD) model [34] to Real-ISR, showcasing the potentials of pre-trained diffusion priors for enhancing the quality of LR images. PASD [55] and SeeSR [48] demonstrate that prompts can better activate the generative capacity of SD models, further improving the visual quality of Real-ISR output. These early SD-based methods employ the LR image as a control signal and start from noise with multi-step denoising to produce outputs, which incur significant computational cost and are prone to hallucination (see Fig. 1). To accelerate inference speed, one-step diffusion-based Real-ISR methods [36, 49, 56, 60, 61] have been proposed, which eliminate random noise initialization by directly taking the LR image as input. However, these methods suffer from limited generative capacity, sacrificing the details of Real-ISR results (see Fig. 1). This motivates us to investigate whether we can find a new training paradigm to improve the generative capacity of one-step diffusion based Real-ISR models.

Recently, Reinforcement Learning (RL) techniques [26, 30, 32, 37, 51], especially those preference optimization algorithms such as Direct Preference Optimization (DPO) [30] and Group Relative Policy Optimization (GRPO) [32], have demonstrated remarkable success in aligning model

*Corresponding author. This research is supported by the PolyU-OPPO Joint Innovative Research Center.

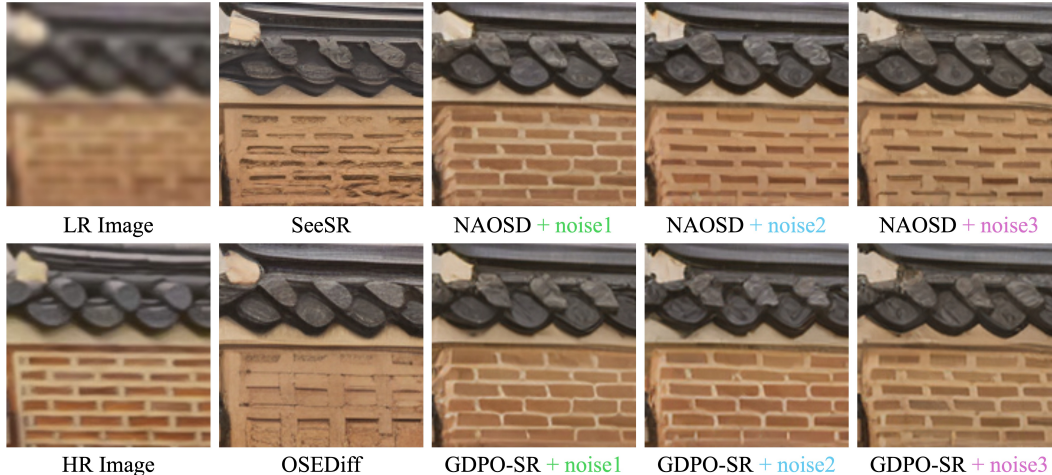


Figure 1. Noise regulates the diversity of generated samples. Different noise inputs yield both high-quality samples (e.g., noise1) and low-quality ones (e.g., noise2 and noise3). After preference learning, the model produces more visually pleasing results.

outputs with human preferences in various tasks, including large language models [32, 57] and image generation [26, 37, 53], etc. Inspired by this, the pioneering work DP²OSR [50] has successfully applied Diffusion-DPO [37] to multi-step generative Real-ISR, reducing hallucinated details while improving visual quality. Therefore, one natural question arises: *Can we leverage RL to enhance the performance of one-step generative Real-ISR models?*

Unfortunately, there are several challenges that hinder the application of DPO and GRPO to one-step Real-ISR models. Firstly, most of the existing one-step models [36, 49, 56, 61] directly map the LR image to its HR counterpart. Such a deterministic nature hinders the application of DPO and GRPO to Real-ISR, *i.e.*, the policy model should be able to generate diverse outputs for the same input. Secondly, existing RL algorithms exhibit limitations when applied to Real-ISR tasks. DPO performs preference optimization using only a single pair of offline-generated positive and negative samples. This inevitably restricts data diversity and limits the model performance. GRPO alleviates this issue by generating multiple samples online and computing the group-relative advantage for each sample, which improves sample efficiency. However, GRPO only calculates the likelihood of the entire image, overlooking the local details of the image, which can degrade the visual quality of the reconstructed images.

To address these challenges, we propose Group Direct Preference Optimization (GDPO), which integrates the advantages of DPO and GRPO, for effective one-step generative super-resolution. First, we introduce a noise-aware one-step diffusion (NAOSD) as the base model to inject controllable noise into the latent features. By sampling different noises, the model generates outputs of varying quality from the same LR input. As shown in Fig. 1, some noise inputs yield high-quality samples, while others produce suboptimal ones. This variability deterministic nature of existing

one-step models and provides the diversity requirement for RL-based optimization. To avoid performance degradation caused by noise injection, we propose an unequal-timestep strategy to decouple the timestep of noise addition from that of diffusion denoising. Then, we present GDPO to combine the strengths of DPO and GRPO by training with online-generated groups of samples.

GDPO consists of two core stages: advantage calculation and policy optimization. In the advantage calculation stage, to effectively distinguish the quality differences among samples within a group, we introduce an attribute-aware reward function (ARF) that adaptively balances fidelity-related and perception-related metrics. In the policy optimization stage, we reformulate the Diffusion-DPO loss [37] to leverage group-relative advantages, prioritizing higher-reward samples while reducing the influence of less desirable ones, effectively combining the precision of DPO with the efficiency of GRPO. As shown in Fig. 1, our proposed GDPO-based Real-ISR model, GDPO-SR in short, reconstructs clear and regular brick textures.

In summary, we introduce GDPO, a novel RL-based framework built upon a noise-aware one-step diffusion model, facilitating controllable output diversity and adaptive preference optimization for Real-ISR. Extensive experiments show that GDPO-SR achieves clearer and more detailed super-resolved images while reducing artifacts compared to existing methods.

2. Related Work

Real-World Image Super-Resolution. Conventional ISR methods [3, 5, 10, 14, 22, 24, 29, 44, 66, 67] mainly focus on enhancing image fidelity by designing advanced network architectures and loss functions, whereas Real-ISR leverages generative priors to improve the perceptual quality of reconstructed images. Conventional Real-ISR approaches [20, 40, 41, 62] mainly employ GAN [10] to enhance per-

ceptual realism, but suffer from training instability and artifacts [23, 35]. Recently, diffusion models [6, 12, 28, 33, 63] have inspired a surge of Real-ISR methods. Early attempts [16, 17, 42, 59] train diffusion models from scratch; for example, ResShift [59] reformulates noise addition as residual shifting to fit Real-ISR task. However, these methods are limited in generative capacity. With the emergence of large-scale pre-trained T2I models such as SD [34] and FLUX [19], researchers have begun to exploit their powerful generative priors for Real-ISR [9, 39, 48, 55]. DiffBIR [25], SeeSR [48], and PASD [55] demonstrate that leveraging SD’s priors through multi-step denoising can substantially improve the visual quality of reconstructed images. Nevertheless, these approaches suffer from high computational cost and hallucination of details. One-step diffusion-based methods [8, 36, 43, 49, 52, 56, 60, 61, 65] adopt distillation losses [8, 43, 45, 58] to transfer the generative capacity of multi-step models into a one-step framework, achieving visually pleasing results within a single step. However, the one-step constraint limits their generative capacity, motivating us to more effectively exploit the generative prior of diffusion models while maintaining efficiency.

Reinforcement Learning for Real-ISR. Two representative reinforcement learning (RL) algorithms are DPO [30] and GRPO [32]. DPO employs offline-generated positive and negative pairs, encouraging the model to prefer the positive one. In contrast, GRPO performs online optimization by generating a group of samples and computing the relative advantage of each sample, guiding the model to favor those with higher advantages. Both DPO and GRPO have been widely adopted in image generative tasks [26, 37]. Diffusion-DPO [37] extends DPO to diffusion models by reformulating the training objective with an evidence lower bound (ELBO), achieving stable preference alignment. Flow-GRPO [26] and DanceGRPO [53] integrate GRPO into diffusion frameworks, updating models based on each sample’s relative advantage and likelihood. Inspired by these works, DP²OSR [50] applies Diffusion-DPO to multi-step Real-ISR. However, Diffusion-DPO relies solely on offline paired data, limiting sample diversity and hindering model performance. Meanwhile, Flow-GRPO and DanceGRPO calculate the likelihood of the entire image, overlooking local details.

3. Preliminaries

Direct Preference Optimization (DPO). DPO [30] directly optimizes a generative policy by maximizing the likelihood of positive responses over negative ones. Diffusion-DPO [37] extends the preference objective from intractable image-level likelihood to the more tractable reverse diffusion trajectory. It formulates a pixel-level constraint over the one-step denoising process, making preference opti-

mization feasible and effective in the diffusion setting:

$$L(\theta) = -\mathbb{E}_{(x_0^w, x_0^l) \sim \mathcal{D}, x_t^w \sim q(x_t^w | x_0^w), x_t^l \sim q(x_t^l | x_0^l)} \log \sigma(-\omega((\|\epsilon^w - \pi_\theta(x_t^w, t)\|_2^2 - \|\epsilon^w - \pi_{ref}(x_t^w, t)\|_2^2) - (\|\epsilon^l - \pi_\theta(x_t^l, t)\|_2^2 - \|\epsilon^l - \pi_{ref}(x_t^l, t)\|_2^2))), \quad (1)$$

where π_θ and π_{ref} are the policy and reference diffusion models, respectively, \mathcal{D} is the dataset of preference pairs, (x_0^w, x_0^l) are the positive and negative images, $x_t = \sqrt{\alpha_t}x_0 + \sqrt{\beta_t}\epsilon$, t is the timestep, ϵ is the random noise, $\alpha_t + \beta_t = 1$, ω is a hyperparameter, and $\sigma(\cdot)$ is the sigmoid function normalizing the preference score.

Group Relative Policy Optimization (GRPO). GRPO [32] estimates the advantage of each sample by comparing the group-relative rewards of outputs generated by the policy model under the same input. Flow-GRPO [26] and DanceGRPO [53] extend this mechanism to flow-matching models by converting the deterministic ODE sampling into an equivalent SDE form to introduce stochasticity, enabling us to compute the likelihood $p(x_t | t, c)$ of the entire image and measure the probability differences across policies:

$$\max_{p_\theta} \mathbb{E}_{\{x_{0:T}^i\}_{i=1}^G \sim p_{\theta_{old}}(\cdot|c)} \left[\sum_{i=1}^G \sum_{t=1}^T \frac{p_\theta(x_t^i | t, c)}{p_{\theta_{old}}(x_t^i | t, c)} A_i \right], \quad (2)$$

where p_θ and $p_{\theta_{old}}$ represent the likelihood of the policy model and old policy model, respectively. G is the group size. A_i is the group-relative advantage for the i -th sample. T is the number of denoising steps. c is the text embedding. For simplicity, Eq. (2) omits the KL regularization term, the clip term, and the normalization factor $\frac{1}{GT}$, which are typically included in practice to stabilize training.

4. Method

We propose Group Direct Preference Optimization (GDPO), a novel RL-based training paradigm for one-step generative ISR. As illustrated in Fig. 2, our framework consists of two key components: (1) a noise-aware one-step diffusion model as the policy model that generates diverse sample groups from the LR input, and (2) the preference optimization that updates the model based on relative advantages within sample groups. The objective of GDPO is to overcome the deterministic limitation of existing one-step Real-ISR methods, which inherently prevent the application of preference optimization algorithms, while simultaneously addressing the limitations of DPO and GRPO; that is, DPO relies on limited preference pairs and GRPO oversees local perceptual quality.

4.1. Noise-Aware One-Step Diffusion Model

To enable diverse generation from deterministic one-step Real-ISR models, we design a noise-aware one-step diffusion (NAOSD) architecture that injects controllable noise

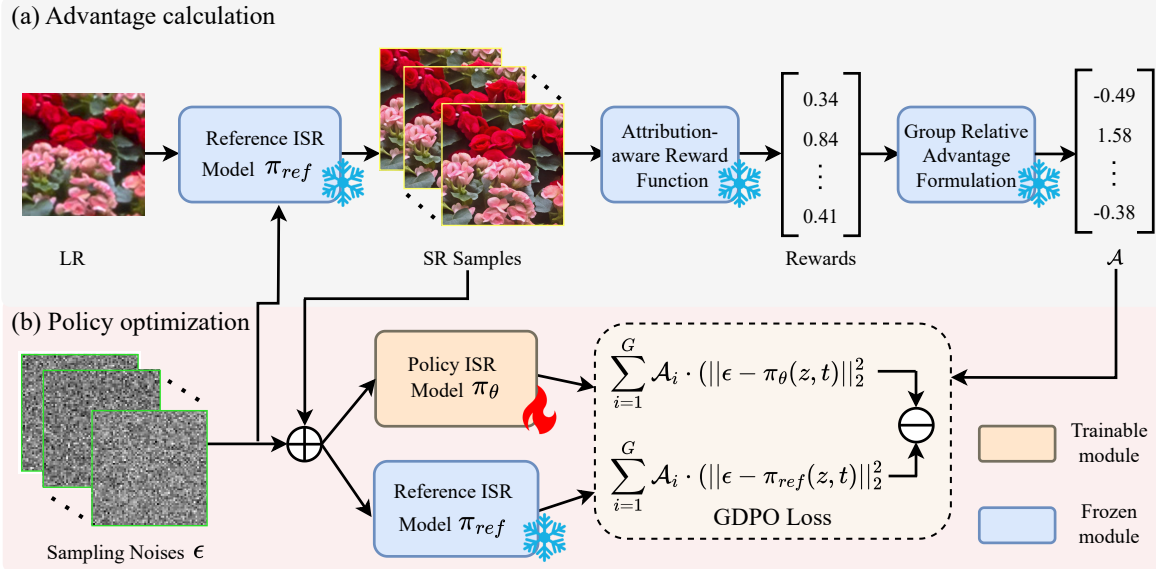


Figure 2. The framework of GDPO, which consists of two core stages: (a) advantage calculation and (b) policy optimization. Firstly, we employ a pre-trained one-step Real-ISR model as the reference model to generate a group of diverse outputs by injecting different random noises. Subsequently, we compute the advantage \mathcal{A} for each sample by evaluating its reward with our designed attribute-aware reward functions and converting these rewards into group-relative advantages. In the policy optimization stage, we feed these samples along with noises into both the policy model and the reference ISR model, and update the parameters of the policy ISR model by minimizing the proposed GDPO loss, steering it to favor generating high-reward samples.

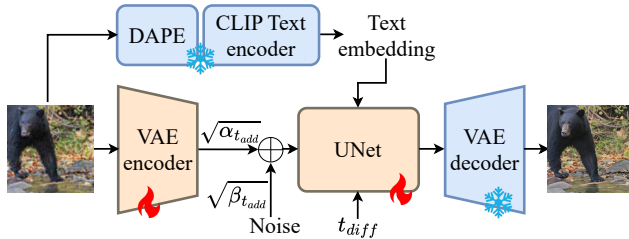


Figure 3. The structure of NAOSD, which uses the t_{add} to control the intensity of injected noise.

into the latent space, as illustrated in Fig. 3. Given an LR input I_{LR} , we first obtain its latent feature $z_{LR} = E(I_{LR})$ through a VAE encoder E . Meanwhile, we derive semantic guidance by extracting a text embedding c_t using a composite prompt extraction module that integrates both DAPE [48] and the CLIP text encoder [31]. To enable stochastic sampling, we inject controllable Gaussian noise ϵ into the latent z_{LR} :

$$\tilde{z} = \sqrt{\alpha_{t_{add}}} z_{LR} + \sqrt{\beta_{t_{add}}} \epsilon, \quad \epsilon \sim \mathcal{N}(0, \mathbf{I}), \quad (3)$$

where $\alpha_{t_{add}} + \beta_{t_{add}} = 1$. The perturbed latent \tilde{z} is then denoised by the UNet at a diffusion timestep t_{diff} , producing the restored latent z_{SR} .

$$z_{SR} = \frac{(\tilde{z} - \sqrt{\beta_{t_{diff}}} \text{UNet}(\tilde{z}, c_t, t_{diff}))}{\sqrt{\alpha_{t_{diff}}}}, \quad (4)$$

where $\alpha_{t_{diff}} + \beta_{t_{diff}} = 1$. Finally, the VAE decoder D maps the restored latent to the super-resolved image $I_{SR} =$

$D(z_{SR})$. Following prior work [49], we employ Low-Rank Adaptation (LoRA) [13] to fine-tune both the VAE encoder and the UNet. The model is trained with a combination of L_1 loss, LPIPS loss and VSD loss:

$$\mathcal{L}_{onestep} = L_1(I_{SR}, I_{HR}) + \lambda_1 L_{LPIPS}(I_{SR}, I_{HR}) + \lambda_2 L_{VSD}(I_{SR}, I_{HR}), \quad (5)$$

where $\lambda_1 = 2$, $\lambda_2 = 1$ are weighting hyper-parameters.

In the above noise-injection and one-step denoising framework, t_{add} determines the injected noise strength and the upper bound of diversity, while t_{diff} governs the denoising strength and reconstruction fidelity. Empirically, if we set $t_{add} = t_{diff}$ and increase the timestep of them, the generative capability of the model improves but the fidelity degrades notably. To balance this trade-off, we propose an unequal-timestep strategy, which set a larger t_{add} to expand the sampling space while adopting a more conservative t_{diff} to stabilize fidelity.

Remark (Diversity induced by the noise). We provide an approximate analysis to show that noise injection preserves a residual stochastic term, enabling diverse outputs. Assuming perfect noise prediction ($\text{UNet}(\tilde{z}, c_t, t_{diff}) \approx \epsilon$), substituting Eq. (3) into Eq. (4) gives the approximate solution:

$$z_{SR} \approx \frac{\sqrt{\alpha_{t_{add}}}}{\sqrt{\alpha_{t_{diff}}}} z_{LR} + \frac{\sqrt{\beta_{t_{add}}} - \sqrt{\beta_{t_{diff}}}}{\sqrt{\beta_{t_{diff}}}} \epsilon. \quad (6)$$

This approximation indicates that when $t_{add} \neq t_{diff}$, an additional noise term ϵ is introduced, increasing diversity.

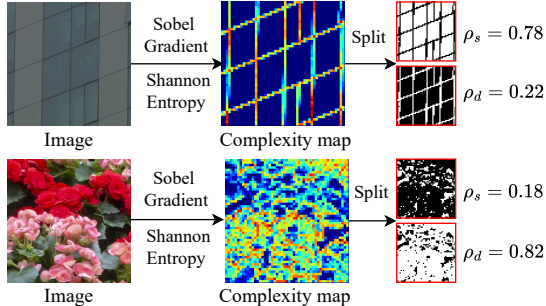


Figure 4. The pipeline of calculating smooth and detailed regions.

4.2. Group Direct Preference Optimization

GDPO utilizes a group of online generated samples to optimize the policy model. As illustrated in Fig. 2, GDPO operates in two sequential stages: *Advantage Calculation*, which computes the relative advantages \mathcal{A} of a group of online generated ISR samples, and *Policy Optimization*, which optimizes the policy model to favor higher-advantage samples. Note that in GDPO, both the reference ISR model π_{ref} and the policy ISR model π_θ are initialized with the pretrained NAOSD model.

Advantage Calculation. For an LR image I_{LR} , we generate a group of G ISR candidates $\mathcal{S} = \{I_{SR}^i\}_{i=1}^G$ by injecting different random noise $\{\epsilon_i\}_{i=1}^G$ into the model. Subsequently, we design an attribute-aware reward function (ARF) to assess each generated sample. Similar to the reward function in DP²O-SR [50], our ARF combines full-reference (FR) metrics (\mathcal{G}_{FR}) and no-reference (NR) metrics (\mathcal{G}_{NR}): the former measure the fidelity to the HR image, while the latter capture perceptual quality. Specifically, in our ARF, \mathcal{G}_{FR} only includes PSNR due to its strong capability to measure image fidelity, while \mathcal{G}_{NR} includes MANIQA [54] and MUSIQ [18] as they are widely used for perceptual quality evaluation.

In addition, different images demand different balances between fidelity and perception—for example, building scenes often favor fidelity, whereas foliage or flower scenes may prioritize perceptual attractiveness. Therefore, we dynamically adjust their weights according to the proportion of smooth and detailed regions in the image. Specifically, we first convert the image to grayscale and partition it into 10×10 patches. For each patch, we compute the Sobel gradient magnitude, build its histogram, and compute the Shannon entropy to measure the complexity of patch details. According to the complexity map, we split the image into smooth regions (low complexity), denoted by Ω_s , and detailed regions (high complexity), denoted by Ω_d , and use their proportions to adaptively weight the reference-based and no-reference rewards:

$$R_i = \rho_s \sum_{f \in \mathcal{G}_{FR}} \frac{s_i^f}{|\mathcal{G}_{FR}|} + \rho_d \sum_{f \in \mathcal{G}_{NR}} \frac{s_i^f}{|\mathcal{G}_{NR}|}, i \in [1 : G] \quad (7)$$

where s_i^f is the min-max normalized score of a metric f (the higher the better). $|\mathcal{G}_{FR}|$ and $|\mathcal{G}_{NR}|$ are the numbers of metrics in \mathcal{G}_{FR} and \mathcal{G}_{NR} , respectively. $\rho_s = \frac{|\Omega_s|}{(|\Omega_s| + |\Omega_d|)}$ and $\rho_d = \frac{|\Omega_d|}{(|\Omega_s| + |\Omega_d|)}$ denote the proportions of smooth and detailed regions, respectively, where $|\Omega_s|$ ($|\Omega_d|$) is the number of pixels in the smooth (detailed) region. Fig. 4 shows the calculation process of smooth and detailed regions.

Reward scores from Eq. (7) reflect each sample’s absolute reward but not their relative reward. We further employ the group relative advantage formulation as in GRPO [32] to compute each sample’s group-relative advantage \mathcal{A}_i , which can inform the model that which candidates are better or worse within the group:

$$\mathcal{A}_i = \frac{R_i - \text{mean}(\{R_j\}_{j=1}^G)}{\text{std}(\{R_j\}_{j=1}^G)}. \quad (8)$$

Policy Optimization. Unlike DPO, which only uses one paired sample, GDPO uses a set of generated samples and the calculated relative advantage \mathcal{A} to update the policy model. The GDPO loss is computed as follows:

$$L_{GDPO} = -\mathbb{E}_{x_0 \sim \mathcal{D}, x_t \sim q(x_t | x_0)} \log \sigma(-\omega \left(\sum_{i=1}^G \mathcal{A}_i (\| \epsilon - \pi_\theta(x_t, t) \|_2^2 - \| \epsilon - \pi_{ref}(x_t, t) \|_2^2) \right)), \quad (9)$$

where x_t is the noisy latent of ISR candidates. We can see that DPO is a special case of our GDPO with $G = 2$. GDPO favors candidates with larger advantages: when sample i has a higher reward, its \mathcal{A}_i increases and carries more weight in $\sum_{i=1}^G \mathcal{A}_i(\cdot)$, making $-\omega \sum_{i=1}^G \mathcal{A}_i(\cdot)$ more likely to be negative, which raises $\log \sigma(\cdot)$ and drives the gradient to prioritize these high-reward samples—achieving alignment biased toward the higher-reward side. In contrast to GRPO, which requires computing the full-image likelihood, GDPO inherits Diffusion-DPO’s advantage of implicit likelihood computation while imposing pixel-level constraints, thereby learning local details more effectively.

5. Experiment

5.1. Experimental Settings

Training Datasets. Similar to previous works [39, 49], our base model NAOSD is pre-trained on 1.5 million 512×512 image patches cropped from the LSDIR dataset [21] and the first 10K face images of the FFHQ dataset [15]. For the GDPO stage, we further select 120,000 high-quality 512×512 image patches from LSDIR for fine-tuning. The Real-ESRGAN degradation pipeline [41] is utilized to construct the low- and high-resolution training pairs.

Testing Datasets. To assess the effectiveness of our proposed GDPO, we adopt the benchmark datasets used in

Table 1. Performance comparison with the base model NAOSD on real-world and synthetic datasets. Metrics with a blue background denote those utilized in the reward function, while yellow-shaded ones correspond to metrics that are excluded from it. Arrows denote if higher (\uparrow) or lower (\downarrow) values represent better performance. The best results are highlighted in **red**.

| Dataset | Method | PSNR \uparrow | SSIM \uparrow | LPIPS \downarrow | FID \downarrow | DISTS \downarrow | MANIQA \uparrow | MUSIQ \uparrow | CLIPQA \uparrow | AFINE \downarrow |
|-----------|---------|-----------------|-----------------|--------------------|------------------|--------------------|-------------------|------------------|-------------------|--------------------|
| DrealSR | NAOSD | 27.97 | 0.7831 | 0.2859 | 140.37 | 0.2113 | 0.6041 | 65.17 | 0.6886 | 20.52 |
| | GDPO-SR | 28.18 | 0.7839 | 0.2851 | 138.87 | 0.2112 | 0.6180 | 65.63 | 0.7020 | 18.72 |
| RealSR | NAOSD | 25.25 | 0.7346 | 0.2689 | 114.91 | 0.2001 | 0.6459 | 69.06 | 0.6617 | 18.90 |
| | GDPO-SR | 25.48 | 0.7328 | 0.2675 | 112.13 | 0.1980 | 0.6615 | 69.42 | 0.6760 | 17.73 |
| DIV2K-val | NAOSD | 23.83 | 0.6131 | 0.2848 | 25.16 | 0.1922 | 0.6297 | 68.20 | 0.6758 | 41.76 |
| | GDPO-SR | 23.92 | 0.6117 | 0.2897 | 26.44 | 0.1965 | 0.6423 | 68.80 | 0.6929 | 41.56 |

Table 2. Quantitative comparison with different methods on real-world and synthetic datasets. The best and second best results are highlighted in **red** and **blue**, respectively. Arrows denote if higher (\uparrow) or lower (\downarrow) values represent better performance.

| Dataset | Method | PSNR \uparrow | SSIM \uparrow | LPIPS \downarrow | FID \downarrow | DISTS \downarrow | MANIQA \uparrow | MUSIQ \uparrow | CLIPQA \uparrow | AFINE \downarrow |
|-----------|----------|-----------------|-----------------|--------------------|------------------|--------------------|-------------------|------------------|-------------------|--------------------|
| DrealSR | StableSR | 28.03 | 0.7536 | 0.3284 | 148.98 | 0.2269 | 0.5592 | 58.51 | 0.6356 | 35.77 |
| | DiffBIR | 26.71 | 0.6571 | 0.4557 | 166.79 | 0.2748 | 0.5927 | 61.07 | 0.6395 | 39.42 |
| | SeeSR | 28.07 | 0.7684 | 0.3174 | 147.39 | 0.2315 | 0.6054 | 65.08 | 0.6905 | 22.79 |
| | PASD | 27.36 | 0.7073 | 0.3760 | 156.13 | 0.2531 | 0.6160 | 64.87 | 0.6808 | 33.89 |
| | OSDiff | 27.92 | 0.7835 | 0.2968 | 135.30 | 0.2165 | 0.5899 | 64.65 | 0.6963 | 21.39 |
| | InvSR | 25.79 | 0.7176 | 0.3471 | 166.42 | 0.2381 | 0.6212 | 64.92 | 0.6918 | 21.69 |
| | GDPO-SR | 28.18 | 0.7839 | 0.2851 | 138.87 | 0.2112 | 0.6180 | 65.63 | 0.7020 | 18.72 |
| RealSR | StableSR | 24.64 | 0.7080 | 0.3002 | 128.51 | 0.2140 | 0.6215 | 65.88 | 0.6234 | 27.62 |
| | DiffBIR | 24.75 | 0.6567 | 0.3636 | 128.99 | 0.2312 | 0.6252 | 64.98 | 0.6463 | 32.64 |
| | SeeSR | 25.15 | 0.7210 | 0.3007 | 125.45 | 0.2224 | 0.6441 | 69.82 | 0.6707 | 24.07 |
| | PASD | 25.21 | 0.6798 | 0.3380 | 124.28 | 0.2260 | 0.6493 | 68.75 | 0.6620 | 39.00 |
| | OSDiff | 25.15 | 0.7341 | 0.2921 | 123.49 | 0.2128 | 0.6326 | 69.09 | 0.6693 | 20.92 |
| | InvSR | 24.30 | 0.7145 | 0.2775 | 129.52 | 0.2060 | 0.6561 | 67.31 | 0.6739 | 16.58 |
| | GDPO-SR | 25.48 | 0.7328 | 0.2675 | 112.13 | 0.1980 | 0.6615 | 69.42 | 0.6760 | 17.73 |
| DIV2K-val | StableSR | 23.26 | 0.5726 | 0.3113 | 24.44 | 0.2048 | 0.6190 | 65.92 | 0.6771 | 49.31 |
| | DiffBIR | 23.64 | 0.5647 | 0.3524 | 30.73 | 0.2128 | 0.6209 | 65.81 | 0.6704 | 49.58 |
| | SeeSR | 23.82 | 0.6096 | 0.3160 | 25.42 | 0.1971 | 0.6187 | 68.50 | 0.6893 | 42.18 |
| | PASD | 23.23 | 0.5877 | 0.3634 | 30.12 | 0.2200 | 0.6420 | 68.41 | 0.6802 | 45.19 |
| | OSDiff | 23.72 | 0.6108 | 0.2941 | 26.32 | 0.1976 | 0.6148 | 67.97 | 0.6683 | 44.69 |
| | InvSR | 23.10 | 0.5985 | 0.3045 | 28.45 | 0.1985 | 0.6406 | 68.43 | 0.7118 | 37.51 |
| | GDPO-SR | 23.92 | 0.6117 | 0.2897 | 26.44 | 0.1965 | 0.6423 | 68.80 | 0.6929 | 41.56 |

previous works [39, 49, 56], including DRealSR [46], RealSR [2] and DIV2K-val [1]. Specifically, RealSR and DRealSR contain 100 and 93 pairs of real-world low- and high-resolution images, respectively, where the LR and HR images are center-cropped to 128×128 and 512×512 . In contrast, DIV2K-val consists of 3,000 synthetic LR-HR pairs of 512×512 resolution, generated using the Real-ESRGAN degradation pipeline.

Implementation Details. The SD2.1-base [31] is used as the pre-trained diffusion model. In the pre-training of our base model NAOSD, we set batch size as 16 and run for 35,000 iterations on 4 NVIDIA A100 GPUs. The AdamW optimizer [27] is used with the the rank of LoRA set to 4 and the learning rate set to 5×10^{-5} . In the GDPO fine-tuning stage, the LoRA rank is also set to 4. The group size of GDPO is set to 6, while the learning rate and batch size are configured to 5×10^{-5} and 8, respectively. The preference weighting hyperparameter ω in Eq. (9) is set to 5,000 and the GDPO-SR model is trained for 1,500 iterations on 8 NVIDIA A100 GPUs.

Evaluation Metrics. The performance of the proposed model is evaluated across a set of widely used image quality

assessment metrics, which are divided into two categories. (1) Metrics included in the ARF, comprising both FR metric PSNR and NR metrics MUSIQ [18] and MANIQA [54]. (2) Metrics not included in the ARF, including FR metrics SSIM [44], LPIPS [64], FID [11] and DISTS [7], and NR metrics CLIPQA [38] and AFINE [47].

Compared Methods. To demonstrate the effectiveness of GDPO-SR, we conduct comparisons against: (1) recent SD-based multi-step Real-ISR methods, including StableSR [39], PASD [55], DiffBIR [25], and SeeSR [48]; (2) one-step diffusion approaches such as OSDiff [49] and InvSR [60]; and (3) the recently developed RL-based Real-ISR method DP²OSR [50].

5.2. Experimental Results

Comparison with Base Model. Table 1 presents a performance comparison between the proposed GDPO-SR and its base model NAOSD. For fairness, NAOSD and GDPO-SR are fed with identical noise for the same input. First, we can see that GDPO-SR consistently achieves better results on all metrics involved in ARF. For instance, on the RealSR dataset, the PSNR increases from 25.25dB to 25.48dB,

Table 3. Quantitative comparison with DP²O-SR on real-world datasets. The best results are highlighted in red.

| Dataset | Method | PSNR \uparrow | SSIM \uparrow | LPIPS \downarrow | FID \downarrow | DISTS \downarrow | MANIQA \uparrow | MUSIQ \uparrow | CLIQQA \uparrow | AFINE \downarrow |
|---------|----------------------|-----------------|-----------------|--------------------|------------------|--------------------|-------------------|------------------|-------------------|--------------------|
| DrealSR | DP ² O-SR | 23.95 | 0.6294 | 0.4412 | 157.76 | 0.2763 | 0.6674 | 71.09 | 0.7842 | 11.39 |
| | GDPO-SR | 28.18 | 0.7839 | 0.2851 | 138.87 | 0.2112 | 0.6180 | 65.63 | 0.7020 | 18.72 |
| RealSR | DP ² O-SR | 22.39 | 0.6467 | 0.3513 | 131.79 | 0.2442 | 0.7036 | 73.24 | 0.7484 | 8.654 |
| | GDPO-SR | 25.48 | 0.7328 | 0.2675 | 112.13 | 0.1980 | 0.6615 | 69.42 | 0.6760 | 17.73 |

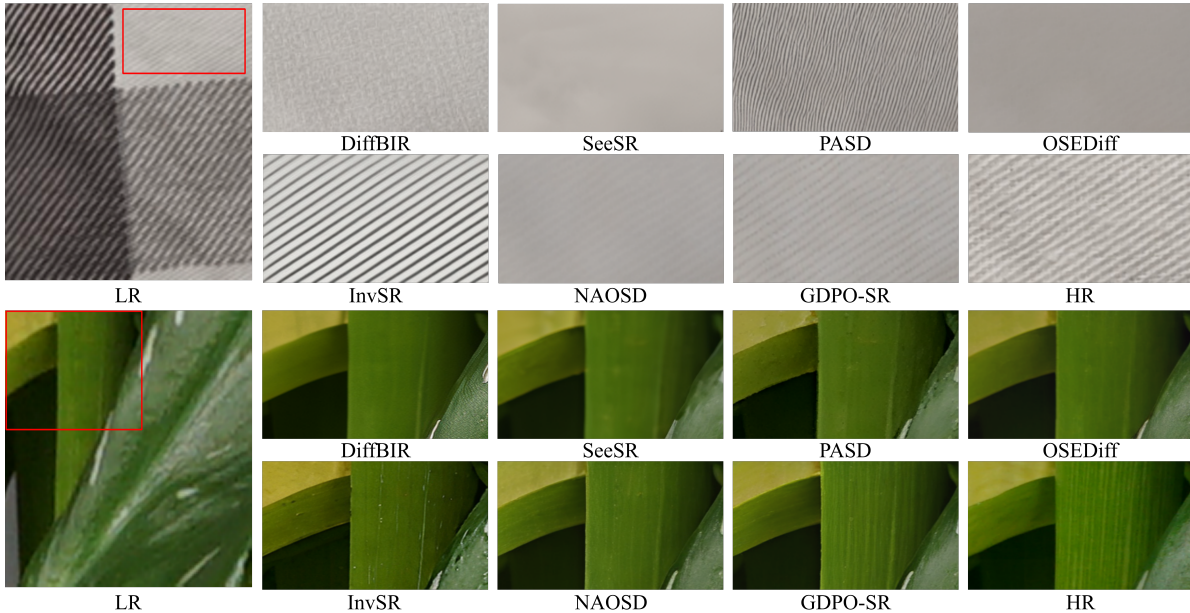


Figure 5. Visual comparison with SD-based Real-ISR methods. Please zoom in for a better view.

while MANIQA improves from 0.6459 to 0.6615, and MUSIQ rises from 69.06 to 69.42. Second, for metrics not included in the ARF, GDPO-SR still outperforms NAOSD, particularly on NR metrics (CLIQQA and AFINE). On the synthetic DIV2K-val dataset, although GDPO-SR does not surpass NAOSD in SSIM, LPIPS, FID and DISTS, it achieves improvements in PSNR and all NR metrics. In particular, GDPO-SR’s advantages on both the real-world datasets (DRealSR and RealSR) highlight its generalization capability under realistic degradations. Overall, GDPO-SR effectively improves the performance of NAOSD, validating the effectiveness of the proposed GDPO strategy.

Comparison with State-of-the-Arts. Table 2 presents a quantitative comparison between GDPO-SR and state-of-the-art SD-based Real-ISR methods on real-world and synthetic datasets. For FR metrics, GDPO-SR achieves the best performance among all methods on PSNR, LPIPS and DISTS across all the three datasets. GDPO-SR also shows leading performance in other FR metrics, such as SSIM and FID, further demonstrating its strong ability to reproduce the fidelity and structure of the images. For NR metrics, GDPO-SR still maintains overall leading performance, confirming that the model not only restores high-fidelity details but also produces visually more natural and pleasing results. Specifically, on the DRealSR dataset, GDPO-SR achieves the highest PSNR (28.18dB), SSIM

Table 4. Comparison of mode size, running-time and FLOPs.

| Methods | StableSR | DiffBIR | SeeSR | PASD | OSDiff | InvSR | GDPO-SR |
|----------|----------|---------|-------|-------|--------|-------|---------|
| Para.(B) | 1.56 | 1.68 | 2.51 | 2.31 | 1.77 | 1.33 | 1.77 |
| Time(s) | 10.03 | 2.72 | 4.30 | 2.80 | 0.11 | 0.12 | 0.11 |
| FLOPs(T) | 79.94 | 24.31 | 65.86 | 29.13 | 2.27 | 2.40 | 2.27 |

(0.7839), MUSIQ (65.63), and CLIQQA (0.7020), while showing the lowest LPIPS (0.2851) and DISTS (0.2112), significantly surpassing both multi-step approaches (*e.g.*, PASD, SeeSR) and one-step methods (*e.g.*, OSDiff, InvSR). These results clearly validate GDPO-SR’s superior reconstruction quality and perceptual realism.

Qualitative Comparisons. The visual comparisons are shown in Fig. 5. One can see that, compared with the base model NAOSD, GDPO-SR produces clearer structures and richer fine details. Compared with other SD-based methods, our GDPO-SR shows clear superiority. In the first example of Fig. 5, GDPO-SR reconstructs fine texture patterns that are more consistent with the HR image, while InvSR produces excessively saturated textures that deviate from the HR image. Similarly, in the second example, GDPO-SR can reconstruct clearer and more realistic plant textures and vein details, while competing methods produce over-smoothed results that lack realistic textures. These qualitative results highlight that GDPO-SR not only enhances image clarity but also preserves realistic and detailed structures, outperforming both the base model and other comparison meth-



Figure 6. Visual comparison with DP²O-SR.

Table 5. Ablation studies on GDPO on the RealSR dataset.

| Method | PSNR \uparrow | FID \downarrow | DISTS \downarrow | MUSIQ \uparrow | AFINE \downarrow |
|---------------|-----------------|------------------|--------------------|------------------|--------------------|
| NAOSD | 25.25 | 114.91 | 0.2001 | 69.06 | 20.52 |
| Diffusion-DPO | 25.41 | 112.87 | 0.2010 | 69.16 | 20.22 |
| DanceGRPO | 25.10 | 113.74 | 0.2049 | 69.95 | 16.52 |
| GDPO (ours) | 25.48 | 112.13 | 0.1980 | 69.42 | 18.72 |

ods. Due to page limit, more visual comparisons can be found in the **Supplementary Materials**.

Compared with RL-based methods. We further compare GDPO-SR with DP²OSR [50], a recent RL-based multi-step Real-ISR method. The quantitative results are presented in Table 3. We see that DP²O-SR achieves better NR metrics but performs poorly on FR metrics. This suggests that DP²O-SR promotes strong generative capability in the price of compromising image fidelity. In contrast, our GDPO-SR, as a one-step diffusion model, achieves a more balanced performance, improving fidelity while maintaining competitive perceptual quality. The qualitative comparison in Fig. 6 confirms this observation. DP²O-SR generates richer but inconsistent details with the HR image. Our GDPO-SR produces more faithful results.

Complexity Analysis. Table 4 provides a comparison of parameter counts (Para.), running time, and FLOPs among different SD-based methods. The running time is the average time over processing 100 512×512 images. From the results, it can be seen that GDPO-SR has the same inference time and FLOPs as OSediff, indicating that the introduction of noise and the application of GDPO do not add any computational overhead. Compared with InvSR, although GDPO-SR has slightly more parameters (1.77B vs. 1.33B), it achieves higher inference efficiency (0.11s vs. 0.12s) and smaller FLOPs (2.27T vs. 2.40T).

5.3. Ablation Study

Effectiveness of GDPO. To demonstrate the effectiveness of the proposed GDPO strategy, we conduct comparisons with other reinforcement learning methods, including diffusion-DPO [37] and DanceGRPO [53]. The results are shown in Table 5. Compared with Diffusion-DPO, our GDPO achieves better performance on both FR and NR metrics, highlighting its advantage in leveraging inter-group online samples for balanced optimization. Compared with NAOSD, DanceGRPO enhances NR metrics but leads to a degradation in FR metrics. It indicates that the global likelihood estimation in DanceGRPO cannot capture local image distributions, causing a deterioration in image fidelity. Overall, our GDPO achieves a favorable balance between

Table 6. Ablation studies on ARF on the RealSR dataset.

| Method | LPIPS \downarrow | DISTS \downarrow | MUSIQ \uparrow | CLIPQA \uparrow |
|------------|--------------------|--------------------|------------------|-------------------|
| NAOSD | 0.2689 | 0.2001 | 69.06 | 0.6617 |
| ARF w/ FR | 0.2642 | 0.1978 | 67.68 | 0.6359 |
| ARF w/ NR | 0.2866 | 0.2102 | 69.80 | 0.6914 |
| ARF w/o AW | 0.2660 | 0.1979 | 68.42 | 0.6331 |
| ARF (ours) | 0.2675 | 0.1980 | 69.42 | 0.6760 |

Table 7. Ablation studies on Group Size on the RealSR dataset.

| G | PSNR \uparrow | DISTS \downarrow | MANIQA \uparrow | CLIPQA \uparrow |
|---------------|-----------------|--------------------|-------------------|-------------------|
| NAOSD | 25.25 | 0.2001 | 0.6459 | 0.6617 |
| GDPO-SR (G=4) | 25.45 | 0.1996 | 0.6491 | 0.6610 |
| GDPO-SR (G=6) | 25.48 | 0.1980 | 0.6615 | 0.6760 |
| GDPO-SR (G=8) | 25.34 | 0.1955 | 0.6619 | 0.6788 |

perceptual quality and fidelity.

Effectiveness of ARF. To verify the effectiveness of different components within ARF, we conducted five ablation experiments in Table 6. ARF w/ FR uses only the FR metric in the reward function, while ARF w/ NR uses only the NR metric. ARF w/o AW removes the adaptive weighting by fixing both ρ_s and ρ_d in Eq. (7) to 0.5. Compared with NAOSD, incorporating only the FR metric (“ARF w/ FR”) improves FR metrics such as LPIPS and DISTS but leads to a noticeable drop in NR metrics. In contrast, using only the NR metric (“ARF w/ NR”) enhances perceptual quality while degrading fidelity. These results suggest that relying solely on either FR or NR metrics is insufficient to evaluate the overall quality of the reconstructed images. Besides, compared with ARF, removing the adaptive weighting (“ARF w/o AR”) results in suboptimal performance across all metrics, indicating that a uniform weighting scheme cannot capture spatially varying characteristics of image content. This demonstrates that adaptively combining FR and NR metrics according to image content provides a reliable evaluation of image quality.

The effect of group size. We conducted four experiments to investigate the effect of group size (G), with G set to 4, 6, and 8, respectively. The results are presented in Table 7. It can be observed that as G increases, the model’s generative capability improves, as indicated by the higher NR metric. This suggests that a larger G leads to more diverse sample generation, thereby enhancing the model’s overall generative performance. In contrast, when G is too small, the limited diversity of samples restricts effective preference learning, resulting in minimal performance gains.

The timestep in NAOSD. To investigate the impact of $t=(t_{add}, t_{diff})$ on NAOSD, we conduct four ablation experiments by settings t as (100,100), (250,250), (500,500) and (250,100). Fig. 7(a) shows the fluctuation range, which is defined as the difference between the maximum and minimum values for each metric, under the four settings. For each setting, we randomly sample 50 outputs per input on the RealSR dataset, yielding 50 values for each metric. As can be seen, when the timestep increases from

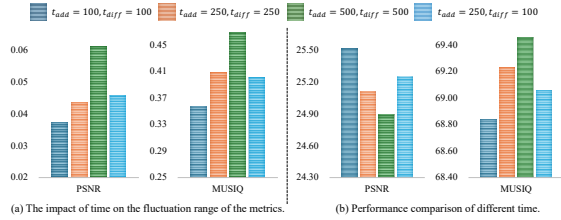


Figure 7. Ablation studies on the timestep setting in NAOSD.

(100,100) to (500,500), both PSNR and MUSIQ exhibit larger fluctuation ranges. This suggests that a larger t introduces more noise into the generation process, which increases randomness and enhances sample diversity. Fig. 7(b) presents the performance comparison across different t . As observed, increasing t enhances the generative ability but compromises fidelity. To address this trade-off, we adopt an unequal-time strategy ($t_{add} = 250, t_{diff} = 100$) to balance fidelity and generative capacity while maintaining a reasonable fluctuation range.

6. Conclusion

In this paper, we proposed Group Direct Preference Optimization (GDPO), a novel RL framework for one-step generative image super-resolution. Specifically, we first presented the NAOSD base model with an unequal-timestep strategy, injecting controllable noise into the latent space to produce diverse outputs. Based on NAOSD, we proposed GDPO, which integrated the strengths of DPO and GRPO to perform online preference optimization using multiple generated samples. To effectively distinguish quality differences among these samples, we designed an attribute-aware reward function that dynamically balanced fidelity-related and perception-related metrics according to the content of smooth and textured regions. Extensive experiments demonstrated that GDPO-SR effectively enhanced both visual quality and structural fidelity, achieving superior performance over existing Real-ISR methods.

Limitations. While GDPO achieves better performance than DPO, it needs to generate multiple outputs for each input during training, which increases training overhead. In addition, ARF provides more reasonable reward scores by adaptively combining FR and NR metrics according to image content, but it remains a manually designed heuristic reward. How to design a reward aligning better with human visual perception deserves more investigation.

References

- [1] Eirikur Agustsson and Radu Timofte. Ntire 2017 challenge on single image super-resolution: Dataset and study. In *Proceedings of the IEEE conference on computer vision and pattern recognition workshops*, pages 126–135, 2017. 6, 14
- [2] Jianrui Cai, Hui Zeng, Hongwei Yong, Zisheng Cao, and Lei Zhang. Toward real-world single image super-resolution: A new benchmark and a new model. In *Proceedings of the IEEE/CVF International Conference on Computer Vision*, pages 3086–3095, 2019. 6, 14
- [3] Du Chen, Liyi Chen, Zhengqiang Zhang, and Lei Zhang. Generalized and efficient 2d gaussian splatting for arbitrary-scale super-resolution. *arXiv preprint arXiv:2501.06838*, 2025. 1, 2
- [4] Du Chen, Tianhe Wu, Kede Ma, and Lei Zhang. Toward generalized image quality assessment: Relaxing the perfect reference quality assumption. In *Proceedings of the Computer Vision and Pattern Recognition Conference*, pages 12742–12752, 2025. 14
- [5] Tao Dai, Jianrui Cai, Yongbing Zhang, Shu-Tao Xia, and Lei Zhang. Second-order attention network for single image super-resolution. In *Proceedings of the IEEE/CVF conference on computer vision and pattern recognition*, pages 11065–11074, 2019. 1, 2
- [6] Prafulla Dhariwal and Alexander Nichol. Diffusion models beat gans on image synthesis. *Advances in neural information processing systems*, 34:8780–8794, 2021. 1, 3
- [7] Keyan Ding, Kede Ma, Shiqi Wang, and Eero P Simoncelli. Image quality assessment: Unifying structure and texture similarity. *IEEE transactions on pattern analysis and machine intelligence*, 44(5):2567–2581, 2020. 6
- [8] Linwei Dong, Qingnan Fan, Yihong Guo, Zhonghao Wang, Qi Zhang, Jinwei Chen, Yawei Luo, and Changqing Zou. Tsd-sr: One-step diffusion with target score distillation for real-world image super-resolution. In *Proceedings of the Computer Vision and Pattern Recognition Conference*, pages 23174–23184, 2025. 3
- [9] Zheng-Peng Duan, Jiawei Zhang, Xin Jin, Ziheng Zhang, Zheng Xiong, Dongqing Zou, Jimmy S Ren, Chun-Le Guo, and Chongyi Li. Dit4sr: Taming diffusion transformer for real-world image super-resolution. *arXiv preprint arXiv:2503.23580*, 2025. 3
- [10] Ian Goodfellow, Jean Pouget-Abadie, Mehdi Mirza, Bing Xu, David Warde-Farley, Sherjil Ozair, Aaron Courville, and Yoshua Bengio. Generative adversarial nets. *Advances in neural information processing systems*, 27, 2014. 2
- [11] Martin Heusel, Hubert Ramsauer, Thomas Unterthiner, Bernhard Nessler, and Sepp Hochreiter. Gans trained by a two time-scale update rule converge to a local nash equilibrium. *Advances in neural information processing systems*, 30, 2017. 6
- [12] Jonathan Ho, Ajay Jain, and Pieter Abbeel. Denoising diffusion probabilistic models. *Advances in neural information processing systems*, 33:6840–6851, 2020. 1, 3
- [13] Edward J Hu, Yelong Shen, Phillip Wallis, Zeyuan Allen-Zhu, Yuanzhi Li, Shean Wang, Lu Wang, and Weizhu Chen. Lora: Low-rank adaptation of large language models. *arXiv preprint arXiv:2106.09685*, 2021. 4
- [14] Justin Johnson, Alexandre Alahi, and Li Fei-Fei. Perceptual losses for real-time style transfer and super-resolution. In *Computer Vision—ECCV 2016: 14th European Conference, Amsterdam, The Netherlands, October 11–14, 2016, Proceedings, Part II 14*, pages 694–711. Springer, 2016. 2
- [15] Tero Karras, Samuli Laine, and Timo Aila. A style-based generator architecture for generative adversarial networks.

- In *Proceedings of the IEEE/CVF conference on computer vision and pattern recognition*, pages 4401–4410, 2019. 5
- [16] Bahjat Kawar, Gregory Vaksman, and Michael Elad. Snips: Solving noisy inverse problems stochastically. *Advances in Neural Information Processing Systems*, 34:21757–21769, 2021. 1, 3
- [17] Bahjat Kawar, Michael Elad, Stefano Ermon, and Jiaming Song. Denoising diffusion restoration models. *Advances in Neural Information Processing Systems*, 35:23593–23606, 2022. 1, 3
- [18] Junjie Ke, Qifei Wang, Yilin Wang, Peyman Milanfar, and Feng Yang. Musiq: Multi-scale image quality transformer. In *Proceedings of the IEEE/CVF International Conference on Computer Vision*, pages 5148–5157, 2021. 5, 6, 14
- [19] Black Forest Labs. Flux. <https://github.com/black-forest-labs/flux>, 2024. 1, 3
- [20] Christian Ledig, Lucas Theis, Ferenc Huszár, Jose Caballero, Andrew Cunningham, Alejandro Acosta, Andrew Aitken, Alykhan Tejani, Johannes Totz, Zehan Wang, et al. Photo-realistic single image super-resolution using a generative adversarial network. In *Proceedings of the IEEE conference on computer vision and pattern recognition*, pages 4681–4690, 2017. 1, 2
- [21] Yawei Li, Kai Zhang, Jingyun Liang, Jiezhang Cao, Ce Liu, Rui Gong, Yulun Zhang, Hao Tang, Yun Liu, Denis Demandolx, et al. Lsdir: A large scale dataset for image restoration. In *Proceedings of the IEEE/CVF Conference on Computer Vision and Pattern Recognition*, pages 1775–1787, 2023. 5
- [22] Jingyun Liang, Jiezhang Cao, Guolei Sun, Kai Zhang, Luc Van Gool, and Radu Timofte. Swinir: Image restoration using swin transformer. In *Proceedings of the IEEE/CVF international conference on computer vision*, pages 1833–1844, 2021. 1, 2
- [23] Jie Liang, Hui Zeng, and Lei Zhang. Details or artifacts: A locally discriminative learning approach to realistic image super-resolution. In *Proceedings of the IEEE/CVF Conference on Computer Vision and Pattern Recognition*, pages 5657–5666, 2022. 1, 3, 14
- [24] Bee Lim, Sanghyun Son, Heewon Kim, Seungjun Nah, and Kyoung Mu Lee. Enhanced deep residual networks for single image super-resolution. In *Proceedings of the IEEE conference on computer vision and pattern recognition workshops*, pages 136–144, 2017. 1, 2
- [25] Xinqi Lin, Jingwen He, Ziyang Chen, Zhaoyang Lyu, Ben Fei, Bo Dai, Wanli Ouyang, Yu Qiao, and Chao Dong. Diffbir: Towards blind image restoration with generative diffusion prior. *arXiv preprint arXiv:2308.15070*, 2023. 3, 6
- [26] Jie Liu, Gongye Liu, Jiajun Liang, Yangguang Li, Jiaheng Liu, Xintao Wang, Pengfei Wan, Di Zhang, and Wanli Ouyang. Flow-grpo: Training flow matching models via online rl. *arXiv preprint arXiv:2505.05470*, 2025. 1, 2, 3
- [27] Ilya Loshchilov and Frank Hutter. Decoupled weight decay regularization. *arXiv preprint arXiv:1711.05101*, 2017. 6
- [28] Long Peng, Wenbo Li, Renjing Pei, Jingjing Ren, Jiaqi Xu, Yang Wang, Yang Cao, and Zheng-Jun Zha. Towards realistic data generation for real-world super-resolution. *arXiv preprint arXiv:2406.07255*, 2024. 3
- [29] Long Peng, Anran Wu, Wenbo Li, Peizhe Xia, Xueyuan Dai, Xinjie Zhang, Xin Di, Haoze Sun, Renjing Pei, Yang Wang, et al. Pixel to gaussian: Ultra-fast continuous super-resolution with 2d gaussian modeling. *arXiv preprint arXiv:2503.06617*, 2025. 2
- [30] Rafael Rafailov, Archit Sharma, Eric Mitchell, Christopher D Manning, Stefano Ermon, and Chelsea Finn. Direct preference optimization: Your language model is secretly a reward model. *Advances in neural information processing systems*, 36:53728–53741, 2023. 1, 3
- [31] Robin Rombach, Andreas Blattmann, Dominik Lorenz, Patrick Esser, and Björn Ommer. High-resolution image synthesis with latent diffusion models. In *Proceedings of the IEEE/CVF conference on computer vision and pattern recognition*, pages 10684–10695, 2022. 4, 6
- [32] Zhihong Shao, Peiyi Wang, Qihao Zhu, Runxin Xu, Junxiao Song, Xiao Bi, Haowei Zhang, Mingchuan Zhang, YK Li, Yang Wu, et al. Deepseekmath: Pushing the limits of mathematical reasoning in open language models. *arXiv preprint arXiv:2402.03300*, 2024. 1, 2, 3, 5
- [33] Yang Song, Jascha Sohl-Dickstein, Diederik P Kingma, Abhishek Kumar, Stefano Ermon, and Ben Poole. Score-based generative modeling through stochastic differential equations. *arXiv preprint arXiv:2011.13456*, 2020. 1, 3
- [34] Stability.ai. Sd. <https://stability.ai/stable-diffusion>, 2021. 1, 3
- [35] Lingchen Sun, Jie Liang, Shuaizheng Liu, Hongwei Yong, and Lei Zhang. Perception-distortion balanced super-resolution: A multi-objective optimization perspective. *IEEE Transactions on Image Processing*, 2024. 1, 3
- [36] Lingchen Sun, Rongyuan Wu, Zhiyuan Ma, Shuaizheng Liu, Qiaosi Yi, and Lei Zhang. Pixel-level and semantic-level adjustable super-resolution: A dual-lora approach. *arXiv preprint arXiv:2412.03017*, 2024. 1, 2, 3
- [37] Bram Wallace, Meihua Dang, Rafael Rafailov, Linqi Zhou, Aaron Lou, Senthil Purushwalkam, Stefano Ermon, Caiming Xiong, Shafiq Joty, and Nikhil Naik. Diffusion model alignment using direct preference optimization. In *Proceedings of the IEEE/CVF Conference on Computer Vision and Pattern Recognition*, pages 8228–8238, 2024. 1, 2, 3, 8
- [38] Jianyi Wang, Kelvin CK Chan, and Chen Change Loy. Exploring clip for assessing the look and feel of images. In *Proceedings of the AAAI Conference on Artificial Intelligence*, pages 2555–2563, 2023. 6, 14
- [39] Jianyi Wang, Zongsheng Yue, Shangchen Zhou, Kelvin CK Chan, and Chen Change Loy. Exploiting diffusion prior for real-world image super-resolution. *arXiv preprint arXiv:2305.07015*, 2023. 1, 3, 5, 6
- [40] Xintao Wang, Ke Yu, Shixiang Wu, Jinjin Gu, Yihao Liu, Chao Dong, Yu Qiao, and Chen Change Loy. Esrgan: Enhanced super-resolution generative adversarial networks. In *Proceedings of the European conference on computer vision (ECCV) workshops*, pages 0–0, 2018. 1, 2
- [41] Xintao Wang, Liangbin Xie, Chao Dong, and Ying Shan. Real-esrgan: Training real-world blind super-resolution with pure synthetic data. In *Proceedings of the IEEE/CVF international conference on computer vision*, pages 1905–1914, 2021. 1, 2, 5, 14

- [42] Yinhuai Wang, Jiwen Yu, and Jian Zhang. Zero-shot image restoration using denoising diffusion null-space model. *arXiv preprint arXiv:2212.00490*, 2022. 1, 3
- [43] Yufei Wang, Wenhan Yang, Xinyuan Chen, Yaohui Wang, Lanqing Guo, Lap-Pui Chau, Ziwei Liu, Yu Qiao, Alex C Kot, and Bihan Wen. Sinsr: Diffusion-based image super-resolution in a single step. *arXiv preprint arXiv:2311.14760*, 2023. 3
- [44] Zhou Wang, Alan C Bovik, Hamid R Sheikh, and Eero P Simoncelli. Image quality assessment: from error visibility to structural similarity. *IEEE transactions on image processing*, 13(4):600–612, 2004. 2, 6
- [45] Zhengyi Wang, Cheng Lu, Yikai Wang, Fan Bao, Chongxuan Li, Hang Su, and Jun Zhu. Prolificdreamer: High-fidelity and diverse text-to-3d generation with variational score distillation. *arXiv preprint arXiv:2305.16213*, 2023. 3
- [46] Pengxu Wei, Ziwei Xie, Hannan Lu, Zongyuan Zhan, Qixiang Ye, Wangmeng Zuo, and Liang Lin. Component divide-and-conquer for real-world image super-resolution. In *Computer Vision—ECCV 2020: 16th European Conference, Glasgow, UK, August 23–28, 2020, Proceedings, Part VIII 16*, pages 101–117. Springer, 2020. 6, 14
- [47] Haoning Wu, Zicheng Zhang, Weixia Zhang, Chaofeng Chen, Liang Liao, Chunyi Li, Yixuan Gao, Annan Wang, Erli Zhang, Wenxiu Sun, et al. Q-align: Teaching Imms for visual scoring via discrete text-defined levels. *arXiv preprint arXiv:2312.17090*, 2023. 6
- [48] Rongyuan Wu, Tao Yang, Lingchen Sun, Zhengqiang Zhang, Shuai Li, and Lei Zhang. Seesr: Towards semantics-aware real-world image super-resolution. *arXiv preprint arXiv:2311.16518*, 2023. 1, 3, 4, 6
- [49] Rongyuan Wu, Lingchen Sun, Zhiyuan Ma, and Lei Zhang. One-step effective diffusion network for real-world image super-resolution. *arXiv preprint arXiv:2406.08177*, 2024. 1, 2, 3, 4, 5, 6
- [50] Rongyuan Wu, Lingchen Sun, Zhengqiang Zhang, Shihao Wang, Tianhe Wu, Qiaosi Yi, Shuai Li, and Lei Zhang. Dp²o-sr: Direct perceptual preference optimization for real-world image super-resolution. *The Thirty-ninth Annual Conference on Neural Information Processing Systems*, 2025. 2, 3, 5, 6, 8
- [51] Tianhe Wu, Jian Zou, Jie Liang, Lei Zhang, and Kede Ma. Visualquality-r1: Reasoning-induced image quality assessment via reinforcement learning to rank. *arXiv preprint arXiv:2505.14460*, 2025. 1
- [52] Rui Xie, Ying Tai, Kai Zhang, Zhenyu Zhang, Jun Zhou, and Jian Yang. Addsr: Accelerating diffusion-based blind super-resolution with adversarial diffusion distillation. *arXiv preprint arXiv:2404.01717*, 2024. 3
- [53] Zeyue Xue, Jie Wu, Yu Gao, Fangyuan Kong, Lingting Zhu, Mengzhao Chen, Zhiheng Liu, Wei Liu, Qiushan Guo, Weilin Huang, et al. Dancegrp: Unleashing grp on visual generation. *arXiv preprint arXiv:2505.07818*, 2025. 2, 3, 8
- [54] Sidi Yang, Tianhe Wu, Shuwei Shi, Shanshan Lao, Yuan Gong, Mingdeng Cao, Jiahao Wang, and Yujiu Yang. Maniqa: Multi-dimension attention network for no-reference image quality assessment. In *Proceedings of the IEEE/CVF Conference on Computer Vision and Pattern Recognition*, pages 1191–1200, 2022. 5, 6, 14
- [55] Tao Yang, Peiran Ren, Xuansong Xie, and Lei Zhang. Pixel-aware stable diffusion for realistic image super-resolution and personalized stylization. *arXiv preprint arXiv:2308.14469*, 2023. 1, 3, 6
- [56] Qiaosi Yi, Shuai Li, Rongyuan Wu, Lingchen Sun, Yuhui Wu, and Lei Zhang. Fine-structure preserved real-world image super-resolution via transfer vae training. *arXiv preprint arXiv:2507.20291*, 2025. 1, 2, 3, 6
- [57] Qiyang Yu, Zheng Zhang, Ruofei Zhu, Yufeng Yuan, Xiaochen Zuo, Yu Yue, Weinan Dai, Tiantian Fan, Gao-hong Liu, Lingjun Liu, et al. Dapo: An open-source llm reinforcement learning system at scale. *arXiv preprint arXiv:2503.14476*, 2025. 2
- [58] Xin Yu, Yuan-Chen Guo, Yangguang Li, Ding Liang, Song-Hai Zhang, and Xiaojuan Qi. Text-to-3d with classifier score distillation. *arXiv preprint arXiv:2310.19415*, 2023. 3
- [59] Zongsheng Yue, Jianyi Wang, and Chen Change Loy. Resshift: Efficient diffusion model for image super-resolution by residual shifting. *arXiv preprint arXiv:2307.12348*, 2023. 1, 3
- [60] Zongsheng Yue, Kang Liao, and Chen Change Loy. Arbitrary-steps image super-resolution via diffusion inversion. In *Proceedings of the Computer Vision and Pattern Recognition Conference*, pages 23153–23163, 2025. 1, 3, 6
- [61] Aiping Zhang, Zongsheng Yue, Renjing Pei, Wenqi Ren, and Xiaochun Cao. Degradation-guided one-step image super-resolution with diffusion priors. *arXiv preprint arXiv:2409.17058*, 2024. 1, 2, 3
- [62] Kai Zhang, Jingyun Liang, Luc Van Gool, and Radu Timofte. Designing a practical degradation model for deep blind image super-resolution. In *Proceedings of the IEEE/CVF International Conference on Computer Vision*, pages 4791–4800, 2021. 1, 2, 14
- [63] Lvmin Zhang, Anyi Rao, and Maneesh Agrawala. Adding conditional control to text-to-image diffusion models. In *Proceedings of the IEEE/CVF International Conference on Computer Vision*, pages 3836–3847, 2023. 1, 3
- [64] Richard Zhang, Phillip Isola, Alexei A Efros, Eli Shechtman, and Oliver Wang. The unreasonable effectiveness of deep features as a perceptual metric. In *Proceedings of the IEEE conference on computer vision and pattern recognition*, pages 586–595, 2018. 6
- [65] Tainyi Zhang, Zheng-Peng Duan, Peng-Tao Jiang, Bo Li, Ming-Ming Cheng, Chun-Le Guo, and Chongyi Li. Time-aware one step diffusion network for real-world image super-resolution. *arXiv preprint arXiv:2508.16557*, 2025. 3
- [66] Yulun Zhang, Kunpeng Li, Kai Li, Lichen Wang, Bineng Zhong, and Yun Fu. Image super-resolution using very deep residual channel attention networks. In *Proceedings of the European conference on computer vision (ECCV)*, pages 286–301, 2018. 1, 2
- [67] Yulun Zhang, Yapeng Tian, Yu Kong, Bineng Zhong, and Yun Fu. Residual dense network for image super-resolution. In *Proceedings of the IEEE conference on computer vision and pattern recognition*, pages 2472–2481, 2018. 1, 2

Supplementary Material to “GDPO-SR: Group Direct Preference Optimization for One-Step Generative Image Super-Resolution”

The following materials are provided in this supplementary file (unless otherwise specified, GDPO-SR adopts $t_{add} = 250$ and $t_{diff} = 100$ during inference):

- A. The average performance comparison between the baseline and GDPO-SR on the RealSR dataset;
- B. Controlling the generative capability of GDPO-SR through the timestep t_{add} ;
- C. Ablation study on FR reward metrics ;
- D. Ablation study on sample generation methods in RL;
- E. More visual comparisons (referring to Sec. 5.2 in the main paper);
- F. Comparisons with GAN-based methods.

A. Average performance comparison

The model exhibits varying performance under different sampling noise. To ensure a fair and reliable comparison, we conduct 50 independent experiments on the RealSR dataset and evaluate the average performance of NAOSD and GDPO-SR. The results, presented in Table 8, show that GDPO-SR achieves superior average performance compared to NAOSD, indicating that the overall performance of the model is enhanced after reinforcement learning.

B. Control of Generative Capability

The generative capability of GDPO-SR can be controlled by adjusting the diffusion timestep t_{add} during inference. This adjustment allows the model to balance fidelity and realism according to different requirements. The quantitative results on the RealSR dataset are presented in Table 10. Note that the GDPO-SR model is fixed, only t_{add} is adjusted during inference, and all variants are fed with the identical noise for the same input. As can be seen, t_{add} provides an effective way to control the model’s generative capability: larger t_{add} lead to higher no-reference metric scores, indicating stronger generative capability.

C. Ablation Study on FR reward metrics

We conducted four experiments on the RealSR dataset to investigate the effect of different FR metrics as reward function, including PSNR, LPIPS, and their combination PSNR+LPIPS. As shown in Table 9, using these FR metrics as rewards consistently improves performance. Since LPIPS is a semantic perceptual metric that is less sensitive to pixel-wise errors, using it alone as the reward results in slight PSNR gains. The combination PSNR+LPIPS alleviates this limitation, achieving a better balance.

D. Ablation Study on Sample Generation Methods in RL

There are various ways to generate multiple samples, such as adjusting the classifier-free guidance (CFG) scale or modifying the diffusion timestep t_{add} . In this paper, GDPO-SR generates multiple samples by altering the injected noise, enabling

Table 8. Performance comparison (averaged over 50 stochastic runs) on the RealSR dataset. Arrows denote if higher (↑) or lower (↓) values represent better performance. The best results are highlighted in **red**.

| Method | PSNR↑ | SSIM↑ | LPIPS↓ | FID↓ | DISTS↓ | MANIQA↑ | MUSIQ↑ | CLIQQA↑ | AFINE↓ |
|---------|--------------|---------------|---------------|---------------|---------------|---------------|--------------|---------------|--------------|
| NAOSD | 25.27 | 0.7354 | 0.2685 | 116.67 | 0.1997 | 0.6458 | 68.85 | 0.6620 | 19.28 |
| GDPO-SR | 25.49 | 0.7336 | 0.2673 | 116.03 | 0.1978 | 0.6607 | 69.21 | 0.6766 | 18.19 |

Table 9. Ablation studies on FR metrics on the RealSR dataset.

| FR | PSNR↑ | DISTS↓ | MANIQA↑ | CLIQQA↑ |
|------------|-------|--------|---------|---------|
| NAOSD | 25.25 | 0.2001 | 0.6459 | 0.6617 |
| PSNR | 25.48 | 0.1980 | 0.6615 | 0.6760 |
| LPIPS | 25.28 | 0.1997 | 0.6605 | 0.6835 |
| PSNR+LPIPS | 25.33 | 0.1970 | 0.6548 | 0.6701 |

Table 10. The impact of t_{add} on the generation capability of GDPO-SR. Arrows denote if higher (\uparrow) or lower (\downarrow) values represent better performance. The best and second best results are highlighted in **red** and **blue**, respectively.

| Method | PSNR \uparrow | SSIM \uparrow | LPIPS \downarrow | DISTS \downarrow | MANIQA \uparrow | MUSIQ \uparrow | CLIQQA \uparrow | AFINE \downarrow |
|---------------------------|-----------------|-----------------|--------------------|--------------------|-------------------|------------------|-------------------|--------------------|
| GDPO-SR ($t_{add}=150$) | 25.85 | 0.7499 | 0.2541 | 0.1938 | 0.6521 | 68.09 | 0.6331 | 19.89 |
| GDPO-SR ($t_{add}=250$) | 25.48 | 0.7328 | 0.2675 | 0.1980 | 0.6615 | 69.42 | 0.6760 | 17.73 |
| GDPO-SR ($t_{add}=350$) | 24.84 | 0.7074 | 0.2900 | 0.2088 | 0.6646 | 70.14 | 0.6994 | 17.41 |

Table 11. Ablation study on sample generation methods on the Real-ISR dataset. Arrows denote if higher (\uparrow) or lower (\downarrow) values represent better performance.

| Method | PSNR \uparrow | SSIM \uparrow | LPIPS \downarrow | DISTS \downarrow | MANIQA \uparrow | MUSIQ \uparrow | CLIQQA \uparrow | AFINE \downarrow |
|-----------------------|-----------------|-----------------|--------------------|--------------------|-------------------|------------------|-------------------|--------------------|
| NAOSD | 25.25 | 0.7346 | 0.2689 | 0.2001 | 0.6459 | 69.06 | 0.6617 | 18.90 |
| GDPO-SR (CFG) | 25.06 | 0.7174 | 0.2782 | 0.2049 | 0.6543 | 69.47 | 0.6815 | 19.61 |
| GDPO-SR (t_{add}) | 25.29 | 0.7294 | 0.2871 | 0.2133 | 0.6477 | 69.46 | 0.6766 | 17.12 |
| GDPO-SR | 25.48 | 0.7328 | 0.2675 | 0.1980 | 0.6615 | 69.42 | 0.6760 | 17.73 |

Table 12. Quantitative comparison between GDPO-SR and the state-of-the-art GAN-based Real-ISR methods on synthetic and real-world datasets. The best and second best results are highlighted in **red** and **blue**, respectively. Arrows denote if higher (\uparrow) or lower (\downarrow) values represent better performance.

| Datasets | Methods | PSNR \uparrow | SSIM \uparrow | LPIPS \downarrow | FID \downarrow | DISTS \downarrow | MANIQA \uparrow | MUSIQ \uparrow | CLIQQA \uparrow | AFINE \downarrow |
|-----------|------------|-----------------|-----------------|--------------------|------------------|--------------------|-------------------|------------------|-------------------|--------------------|
| DIV2K-val | RealESRGAN | 24.29 | 0.6371 | 0.3112 | 37.64 | 0.2141 | 0.5501 | 61.06 | 0.5277 | 56.20 |
| | BSRGAN | 24.58 | 0.6269 | 0.3351 | 44.23 | 0.2275 | 0.5247 | 61.20 | 0.5071 | 62.21 |
| | LDL | 23.83 | 0.6344 | 0.3256 | 42.29 | 0.2227 | 0.5350 | 60.04 | 0.5180 | 53.19 |
| | GDPO-SR | 23.92 | 0.6117 | 0.2897 | 26.44 | 0.1965 | 0.6423 | 68.80 | 0.6929 | 41.56 |
| RealSR | RealESRGAN | 25.69 | 0.7616 | 0.2727 | 135.18 | 0.2063 | 0.5487 | 60.18 | 0.4449 | 39.53 |
| | BSRGAN | 26.39 | 0.7654 | 0.2670 | 141.28 | 0.2121 | 0.5399 | 63.21 | 0.5001 | 45.69 |
| | LDL | 25.28 | 0.7567 | 0.2766 | 142.71 | 0.2121 | 0.5485 | 60.82 | 0.4477 | 38.43 |
| | GDPO-SR | 25.48 | 0.7328 | 0.2675 | 112.13 | 0.1980 | 0.6615 | 69.42 | 0.6760 | 17.73 |
| DrealSR | RealESRGAN | 28.64 | 0.8053 | 0.2847 | 147.62 | 0.2089 | 0.4907 | 54.18 | 0.4422 | 39.97 |
| | BSRGAN | 28.75 | 0.8031 | 0.2883 | 155.63 | 0.2142 | 0.4878 | 57.14 | 0.4915 | 44.87 |
| | LDL | 28.21 | 0.8126 | 0.2815 | 155.53 | 0.2132 | 0.4914 | 53.85 | 0.4310 | 39.06 |
| | GDPO-SR | 28.18 | 0.7839 | 0.2851 | 138.87 | 0.2112 | 0.6180 | 65.63 | 0.7020 | 18.72 |

diverse outcomes from a single input. To investigate the effects of different sample generation methods, we conduct an ablation study on the Real-ISR dataset, as shown in Table 11. GDPO-SR-CFG denotes the variant that generates samples by changing the CFG, while GDPO-SR- t_{add} represents the variant by varying t_{add} . As shown in Table 11, both the CFG-based and timestep-based sampling methods lead to notable improvements in no-reference metrics; however, they tend to degrade full-reference metrics. In contrast, generating multiple samples with different noises yields more consistent improvements across both no-reference and full-reference metrics.

This is mainly because, when generating multiple samples, changing the CFG or t_{add} introduces an inherent trade-off between fidelity and perceptual quality rather than improving both simultaneously. As demonstrated in Table 10, increasing t_{add} enhances perceptual quality (as reflected by higher no-reference metric scores) but degrades fidelity (as indicated by lower full-reference metric scores), and vice versa. Empirically, adjusting the CFG exhibits a similar trend: higher CFG values tend to improve perceptual quality while reducing fidelity. In contrast, altering the noise can generate richer and more natural variations among samples, including rare but valuable cases that simultaneously achieve high fidelity and high perceptual quality. Due to the existence of these rare samples, generating multiple samples with different noises can simultaneously enhance the model’s generative capability and fidelity.

E. More Visual Comparisons

We provide more visual comparisons in Fig. 8 to demonstrate the effectiveness of GDPO-SR. Firstly, compared with the base model NAOSD, the post-training method GDPO-SR reconstructs sharper and clearer textures (as shown in the first

and second cases) and generates finer details (as seen in the third and fourth cases). Secondly, compared to other advanced SD-based methods, GDPO-SR also exhibits notable advantages. For instance, in the second case, GDPO-SR successfully restores the characters “a” and “y”, whereas other methods struggle to produce accurate shapes. Overall, GDPO-SR delivers sharper structures and more natural details, demonstrating strong robustness and generalization in real-world scenarios.

F. Comparisons with GAN-based Methods

We compare GDPO-SR with three representative GAN-based Real-ISR methods: RealESRGAN [41], BSRGAN [62] and LDL [23]. The quantitative results are summarized in Table 12. As observed, GDPO-SR achieves the best performance on most no-reference metrics (MANIQA [54], MUSIQ [18], CLIPIQA [38], and AFINE [4]) across all the three test datasets (DIV2K-val [1], RealSR [2], and DRealSR [46]). For full-reference metrics (*e.g.*, LPIPS, DISTs, and FID), GDPO-SR also delivers competitive results. The visual comparisons are illustrated in Fig. 9. It can be clearly found that the proposed GDPO-SR method can generate more realistic details than those GAN-based methods. These results demonstrate that GDPO-SR effectively balances fidelity and perceptual quality, surpassing GAN-based counterparts in overall visual realism and quantitative performance.

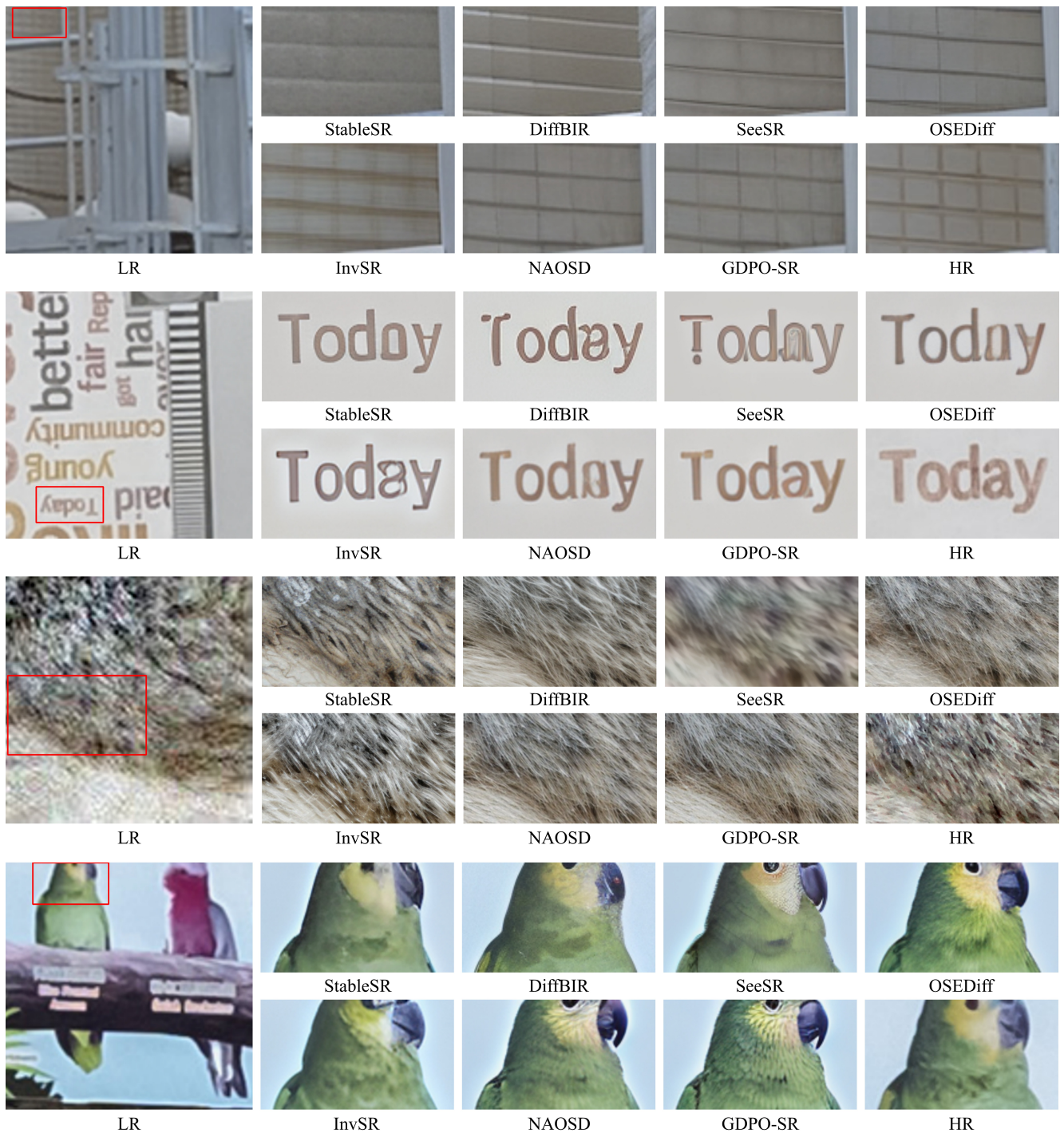


Figure 8. Visual comparison with SD-based Real-ISR methods. Please zoom in for a better view.

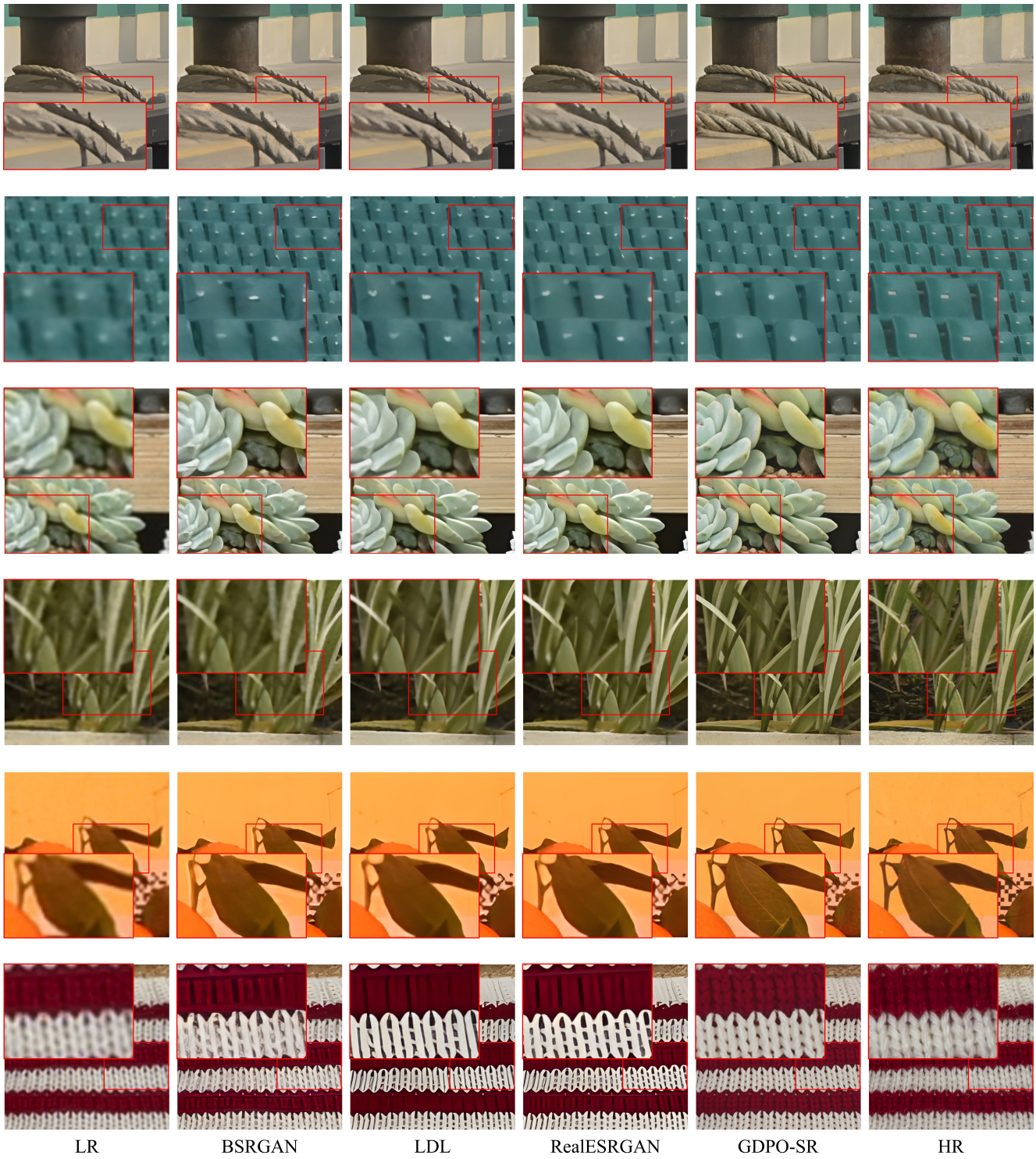


Figure 9. Visual comparison with GAN-based Real-ISR methods. Please zoom in for a better view.